Molecular-Level Insights into Oxygen Reduction Catalysis by Graphite-Conjugated Active Sites

Nathan D. Ricke, Alexander T. Murray, James J. Shepherd, Matthew G. Welborn, Tomohiro Fukushima, Troy Van Voorhis,* and Yogesh Surendranath*,

Department of Chemistry, Massachusetts Institute of Technology, 77 Massachusetts Avenue, Cambridge, Massachusetts 02139, USA

KEYWORDS N-doped carbon, oxygen reduction, electrocatalysis, mechanistic studies, density functional theory

ABSTRACT: Using a combination of experimental and computational investigations we assemble a consistent mechanistic model for the oxygen reduction reaction (ORR) at molecularly well-defined graphitic-conjugated catalyst (**GCC**) active sites featuring aryl-pyridinium moieties (**N^+-GCC**). ORR catalysis at glassy carbon surfaces modified with **N^+-GCC** fragments displays near first order dependence in O_2 partial pressure and near zero order dependence on electrolyte pH. Tafel analysis suggests an equilibrium one-electron transfer process followed by a rate-limiting chemical step at modest overpotentials that transitions to a rate-limiting electron transfer sequence at higher overpotentials. Finite-cluster computational modelling of the **N^+-GCC** active site reveals preferential O_2 adsorption at electrophilic carbons alpha to the pyridinium moiety. Together, the experimental and computational data indicate that ORR proceeds via a proton-decoupled O_2 activation sequence involving either concerted or step-wise electron transfer and adsorption of O_2, which is then followed by a series of electron/proton transfer steps to generate water and turnover the catalytic cycle. The proposed mechanistic model serves as a roadmap for the bottom-up synthesis of highly active N-doped carbon ORR catalysts.

Introduction

The interconversion of water and O_2 is a central chemistry underlying the storage in and release of electricity from energy dense chemical bonds.[1–12] The reduction of O_2 to water provides the oxidizing equivalents to drive fuel combustion in aerobic fuel cells and presents the principal efficiency bottleneck in low temperature fuel cells.[13] This kinetically demanding four-proton, four-electron process is typically executed by platinum group metals in contemporary devices, but the high cost and low terrestrial abundance of precious metals impedes widespread deployment of fuel cell technologies.[12–16] Thus, the development of low-cost, earth abundant cathode catalysts for the oxygen reduction reaction (ORR) presents an essential underlying scientific challenge for enabling a future renewable energy economy.

Nitrogen doped (N-doped) carbon materials have emerged as potentially viable replacements for platinum in low temperature fuel cells.[6,17–31] These materials are typically prepared via high temperature pyrolysis of carbon and nitrogen precursors, and therefore display a large distribution of nitrogen moieties.[21,32,33] The intrinsic heterogeneity of the active sites in these materials has impeded repeated attempts to uncover their mechanism of action and systematically improve their performance.[7,29,34–39] In particular, the sites that bind O_2 are the subject of ongoing debate[7,33–36,40] and knowledge their local molecular structure is essential for the rational synthesis of improved surface active sites with optimal O_2 activation kinetics.

In addition to ambiguity about the site of O_2 activation, the extent of proton coupling in this step remains largely unknown. The dependence of O_2 activation on the nature of proton donors in the medium is of particular relevance to the design of practical devices because polymer electrolyte membrane fuel cells typically operate in acidic media, but metal-free N-doped carbons only display low overpotential catalysis in alkaline electrolytes.[41–43] The specific requirements for making these N-doped carbon ORR catalysts operate more efficiently at lower pH remains largely unknown, and must be remediated in order to utilize these materials in practical devices.

Importantly, N-doped carbon materials are unique in containing active site moieties that resemble well-known organic functional groups (pyridines, pyrroles, imines, amides, nitriles, etc.)[21] which are themselves inactive for the ORR as discrete molecular fragments.[44,45] Thus, a detailed investigation of the complex chemistry of N-doped carbons requires a synthetic strategy that can simultaneously control the local structure of the N-moieties in the material while also reflecting the unique hybrid electronic structure of N-dopant sites embedded within the delocalized band structures of the graphitic carbon host lattice.

Recently, we have developed a mild synthetic route for conjugating designer N-doped molecular fragments to graphitic carbon surfaces.[45] This methodology exploits the native surface chemistry of carbon by condensing substituted 1,2-phenylene diamines site selectively onto o-quinone moieties found ubiquitously at arm-chair edge defects of graphite.[46,47] A combination of XPS, nitrogen K-edge X-ray absorption near edge structure (XANES) spectroscopy, and electrochemical data establish that this mild condensation chemistry generates a uniform array of pyrazine linked molecular cofactor active sites. The robust aromatic linkages formed by this method allow for strong electronic interaction between the incorporated species and the delocalized band structure of graphite, providing an rich experimental platform for connecting molecular and heterogeneous electrocatalysis. We have shown that this functionalization method generates graphite-conjugated catalysts (**GCCs**) that display high activity for the ORR in alkaline aqueous media, and that the activity of these **GCCs** is sensitive to the structure of the molecular fragment incorporated.[45,48]

Our initial synthetic studies of structure-activity correlations on **GCCs** identified carbon surfaces treated with aryl- pyridinium-substituted diamines, dubbed **N$^+$-GCCs**, to be particularly active for the ORR (Scheme 1).[45] With well-defined catalytic sites and appreciable activity, **N$^+$-GCCs** are an ideal platform for detailed experimental investigations of the kinetics of ORR catalysis.

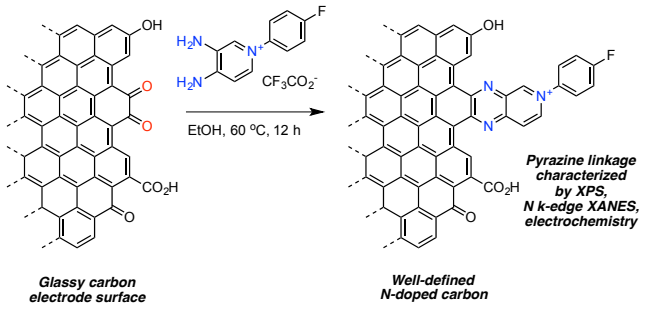

Scheme 1. Synthesis of N$^+$-GCC catalyst by condensation

Additionally, knowledge of the local structure of the incorporated active sites facilitates detailed computational modeling of the energetics of individual reaction steps in the catalytic cycle for ORR. Here we combine electrochemical kinetic studies of these designer surfaces with detailed computational investigations to uncover a consistent mechanistic model for ORR mediated by the incorporated N-dopant sites. In particular, our findings suggest that electrophilic iminium carbons are the sites of preferential O_2 binding and activation, which occurs in a largely pH independent fashion.

Results and discussion

Electrochemical Kinetics of N$^+$-GCCs

Glassy carbon electrodes were pre-oxidized to increase the surface population of *o*-quinone sites, and subsequently treated with the diamine in Scheme 1 to generate **N$^+$-GCC**. This methodology is similar to our previous report and full experimental details of electrode preparation are provided in the SI.[45]

To examine the electrokinetic profile of these modified surfaces for ORR, we collected potentiostatic current-potential (Tafel) data across a range of potentials (0.83 – 0.65 V; unless otherwise stated, all potentials are reported versus the reversible hydrogen electrode, RHE) spanning the catalytic wave, which correspond to overpotentials ranging from 0.40 to 0.58 V. All data were collected with electrode rotation at 2000 rpm to minimize transport limitations. Data at higher overpotentials were also explicitly corrected for residual transport limitations by extrapolating Koutecky-Levich (KL) plots of the reciprocal of the current density, j^{-1}, versus the reciprocal square root of the rotation rate, $\omega^{-1/2}$, to the y-intercept, corresponding to infinite rotation rate, to determine the activation-controlled current density (Figure S1). As previously reported, we observe a slope of approximately 60 mV per decade at the foot of the catalytic wave.[45] At higher overpotentials beyond ~0.7 V vs. RHE, the Tafel slope rises towards ~120 mV per decade (Figure 1). The low overpotential data is consistent with a reversible one-electron transfer followed by a rate-controlling chemical step for O_2 reduction catalysis. The transition to higher Tafel slopes at higher overpotentials could indicate a change in mechanism that is reflective of a sequence involving rate-limiting electron transfer.[49] However, the limited range of Tafel data collection available in the high overpotential region prior to the significant onset of transport limitations impedes an unambiguous determination of the kinetic profile in this region.

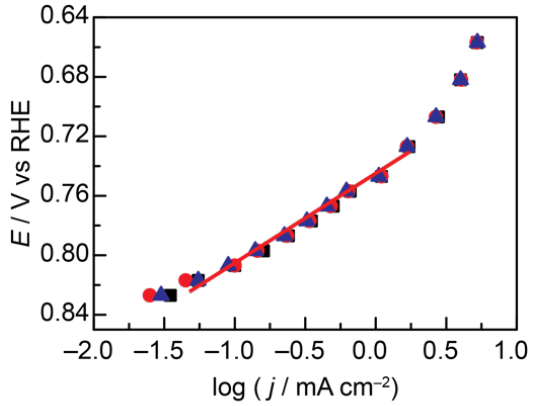

Figure 1. ORR current density-voltage (Tafel) behavior of **N$^+$-GCC** in O_2 – saturated 0.1 M NaOH electrolyte (three runs, single electrode). The red line has a slope of 60 mV/decade and serves as a guide to the eye.

To probe the dependence of ORR on the partial pressure of O_2, we determined the steady state catalytic current at a constant applied potential of 0.71 V at pH 13 over a range of O_2 partial pressures (Figure 2a). We observed an experimental slope of 0.83. Although the reaction order is slightly below

unity, the data is most consistent with a mechanism that involves O_2 activation in the steps leading between the resting state and the rate-limiting step of catalysis.

To probe the pH dependence of this reaction, we examined ORR catalysis mediated by **N$^+$-GCC** electrodes in aqueous $NaClO_4$ electrolyte over the pH range 11-14. All data were collected at constant ionic strength. The ORR catalytic current was held constant at 50 μA cm^{-2} and the potential necessary to maintain this rate was tracked as a function of pH. The data exhibits a very weak pH dependence – on a pH independent normal hydrogen electrode (NHE) scale, the potential changes by ~0.04 V over this 3 pH unit range (Figure 2b). As the overall reactions of ORR to produce either water or peroxide require an equal number of electrons and protons, the thermodynamic potentials scale, according to the Nernst equation, by 60 mV per pH unit. However, catalysis for **N$^+$-GCC** scales by an average of ~10 mV per pH unit over this range, such that ORR requires a greater overpotential at lower pH. This is generally consistent with the phenomenological observation that metal-free N-doped carbons require larger overpotentials in acid electrolytes relative to alkaline media.[43] The observed sub-Nernstian variation of catalysis implies negligible proton coupling in any quasi-equilibrium steps between the resting state and the rate-limiting step of catalysis but does not exclude the participation of water as a proton donor in the rate-limiting step.

Whereas catalysis is weakly dependent on proton activity we do observe a dependence on cation activity. It is difficult to extract an explicit reaction order in cation concentration because the interfacial electric field induces a non-linear variation in local cation activity at the double layer relative to changes in the bulk activity.[49] Nevertheless, increasing the sodium cation concentration from 0.1 M to 1 M leads to a ~1.5x increase in current density at constant potential, implying that cations in the double layer may play a pronounced role in stabilizing charge buildup upon O_2 activation.

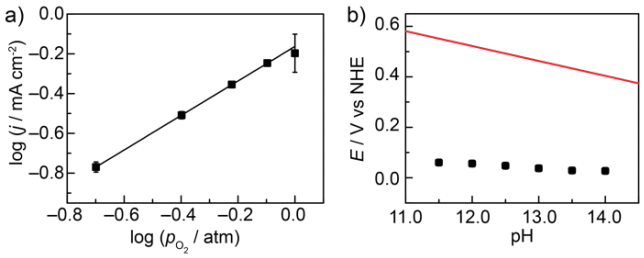

Figure 2. a) P_{O2} – dependence of the O_2 current density at 0.71 V vs. RHE at pH 13 (slope = 0.83) b) Potential (black squares) required to sustain 50 μA cm^{-2} current density for ORR as a function of pH as a function of pH. Data collected in pH – adjusted 1 M $NaClO_4$ electrolyte. Red line indicates the thermodynamic potential of ORR.

Based on the above electrokinetic data, we empirically assemble the following approximate electrochemical rate expression for ORR catalysis on **N$^+$-GCC** modified carbon surfaces:

$$j = j_0[O_2]\exp\left(\frac{bEF}{RT}\right) \qquad \text{eq. } \mathbf{1}$$

Where j_0 is the extrapolated exchange current density for ORR catalysis, b is the empirical electrochemical transfer coefficient, E is the applied potential, F is Faraday's constant, and all other symbols take their usual meaning. We find an observed transfer coefficient of unity, b = 1.0, at higher potentials, corresponding to lower overpotentials, that appears to fall to a b of ~ 0.5 at lower potentials, corresponding to higher overpotentials, beyond 0.7 V. The expression also contains a nominally first order dependence in O_2 activity, which is in line with the experimental data in Figure 2a. This empirical rate expression serves as the basis for comparison to the theoretical model constructed below.

O_2 Binds Preferentially to an Iminium Carbon on the N$^+$-GCC Fragment

We used free energies calculated from density functional theory (DFT)[50,51] to examine possible sites for O_2 activation on **N$^+$-GCC** fragments.

We performed DFT calculations using a cluster model for **N$^+$-GCC** active sites. In order to capture salient aspects of the electron delocalization between the appended nitrogenous fragment and the bulk carbon electrode surface in GCCs, our cluster model includes the nitrogen moiety conjugated with a 14-ring polycyclic aromatic fragment (Figure 3). Although the graphitic domains of the carbon electrodes are generally significantly larger that this 14-ring cluster, we found that varying the graphite region between 1 and 14 rings (Figure S2) led to variations in the energetics of the cycle that were, in most cases, smaller than the DFT error (see Supporting Information for details). Thus, we chose the 14-ring cluster to balance computational cost with inaccuracy arising from edge effects. We note that one could alternatively simulate the catalyst in a periodically replicated unit cell, for example by employing plane wave DFT, which would have the advantage of more properly treating edge effects, but improperly treating the active site as a periodic array of defects. These differences, however, have been shown to be relatively minor for similar systems,[52] so we will restrict ourselves to the cluster model for this study.

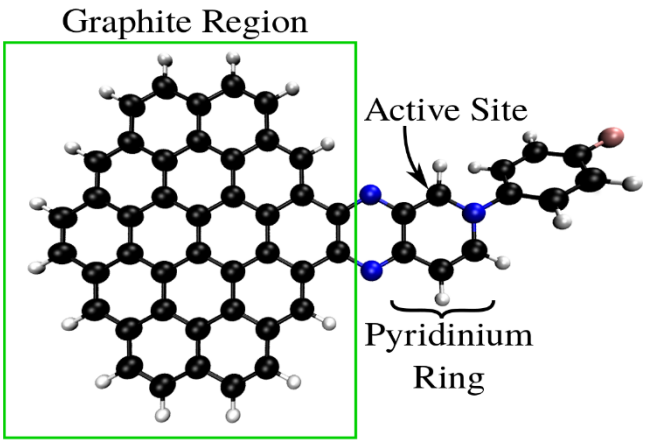

Figure 3. The reduced cluster model of **N$^+$-GCC** with 14 rings in the graphite region.

We calculated DFT free energy changes of all putative elementary reaction steps by calculating the energetics of relevant intermediates with the software package Q-Chem,[53] using the hybrid functional B3LYP,[54,55] and a polarizable continuum model, IEF-PCM[56,57] with a dielectric constant of 78.4. We used implicit solvation in order to reduce computational cost, thereby permitting the calculation of larger clusters. The basis set used was 6-31+G(d).[58–61] We computed entropy contributions to the energies at ambient temperature via frequency analysis, and used the enthalpy and entropy outputs to calculate free energies of formation for all relevant intermediates using an established protocol (see Supporting Information for details).[62,63]

To identify candidate sites for O_2 chemisorption, we computed reaction free energies for O_2 binding to each carbon and nitrogen atom in the **N$^+$-GCC** fragment. While we were unable to identify any local minima for O_2 binding to the **N$^+$-GCC** fragment, upon addition of an electron to the system to form a doublet state, **[N-GCC]$^\bullet$**, we are able to identify local-minima for O_2 binding at each of the two carbons alpha to the aryl iminium nitrogen. O_2 binding to these sites is thermodynamically unfavorable by 0.3 and 1.2 eV with the carbon adjacent to the pyrazine ring being the preferred site of adsorption (Figure 4). This initial computational screening of viable binding configurations suggests that O_2 adsorption is only viable from a doublet ground state and is preferred at electrophilic iminium sites. Importantly, at the surface of the graphitic carbon, N-GCC fragments are conjugated to the band states of the metallic electrode, and therefore **N$^+$-GCC** and **[N-GCC]$^\bullet$** are, in effect, resonance forms or valance tautomers of the same surface moiety. Thus, we use the optimal binding position identified here for **[N-GCC]$^\bullet$** as the basis for further computational investigations of the catalytic cycle.

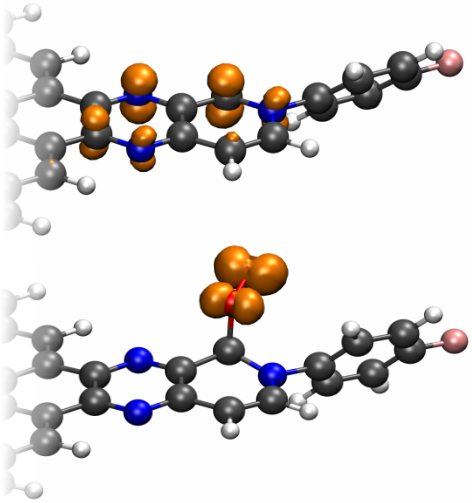

Figure 4. Excess spin density isosurfaces (at an isovalue of 0.01). for **[N-GCC]$^\bullet$** (top) and **[N-GCC-O$_2$]$^\bullet$** (bottom).

Computational spin density analysis provides insight into the origin of this site preference for O_2 binding. Spin density plots of **[N-GCC]$^\bullet$** cluster reveal a preferential accumulation of radical character on the iminium carbon proximal to the pyrazine ring, the preferred site of O_2 adsorption (Figure 4), relative to the distal iminium carbon. This carbon-centered spin density is stabilized by exchange with radical density on the nearby pyrazinic nitrogens of the GCC linkage to the carbon surface. The excess electron also leads to a substantial reduction in the aromatic character of the pyridinium ring: the bond between the active carbon and the iminium nitrogen expands from 1.35 to 1.39 Å upon one electron reduction. In contrast, the bond to the other α-carbon remains 1.38 Å for both species. Notably, one electron reduction does not substantially disrupt the aromaticity of the pyrazine ring, with the average bond length between carbon and pyrazinic nitrogens increasing by less than 0.01 Å. Notably, GCC units lacking the iminium moiety do not display appreciable accumulation of carbon-centered radical character (Figure S3), suggesting that the iminium moiety in **N$^+$-GCC** is uniquely responsible for radical localization on the alpha carbon. Additionally, substitution of the iminium nitrogen for a carbon atom *in silico* serves to eliminate the local minimum for O_2 binding at the corresponding alpha carbon. Radical localization allows the aromatic system to be more easily broken when O_2 binds to this site, which could account for the particularly oxygen binding strength observed for **N$^+$-GCC** surfaces relative to GCC surfaces lacking the pyridinium ring.[45] Importantly, upon O_2 adsorption, the spin density in the GCC transfers completely to the bound O_2 (Figure 4), priming it for further reduction along the catalytic cycle.

Thermodynamic Landscape of ORR Catalysis

The thermodynamic landscape for ORR catalysis on **N$^+$-GCC** moieties was mapped by calculating the free energies of formation for candidate intermediates bound to the iminium carbon sites identified above in the initial computational survey. Our study considered a variety of putative adsorbed oxide intermediate species in varying protonation states. For all cases in which the transition between one intermediate and another involved electron transfer, these free energies were converted to standard reduction potentials versus the reversible hydrogen electrode (RHE) at pH 13 to correspond to the experimental conditions of catalysis. Importantly, transitions between intermediates that involve an equal number of protons and electrons display potentials that are invariant with pH relative to the RHE. In contrast, catalytic steps that involve electron transfer without proton transfer remain pH invariant on a pH independent reference scale (e.g. SHE), but they become effectively pH dependent on an RHE scale because this reference potential scale moves more negative by 59 mV per increment in pH. These calculated redox potentials and free energy changes for chemical steps were used to assemble a viable mechanistic model for ORR catalysis. The thermodynamic analysis reveals that **[N-GCC]$^\bullet$** is the likely resting state of the catalyst and that the initial steps of O_2 activation are far more thermodynamically unfavorable than subsequent reduction events. Thus, we consider the O_2 activation steps in detail before discussing the remainder of the steps in the ORR catalytic cycle.

O_2 Activation (Steps 1 and 2): The localized spin density on **[N-GCC]$^\bullet$** permits several distinct pathways for reaction with O_2, which all display similar thermodynamics in alkaline aqueous media (Scheme 2). Path A of Scheme 2 is depicted in Figure 4, and involves direct adsorption of triplet O_2 with **[N-GCC]$^\bullet$** surface sites. This chemical reaction is disfavored by 0.3 eV, but the resulting adsorbed O_2 is computed to undergo favorable electron-proton transfer with a formal potential of 1.0 V, >0.15 V positive of the onset of ORR catalysis. Given the strong driving force for the proton and electron transfer step, relative to binding O_2, we would expect that the initial chemical O_2 adsorption step is rate-limiting along this pathway. A purely chemical binding of O_2, however, would not display any appreciable potential dependence, which is inconsistent with the strong potential dependence of ORR catalysis observed experimentally (Figure 1). This suggests that the process of binding O_2 instead occurs electrochemically.

We have identified two possible electrochemical pathways for O_2 activation. O_2 activation may proceed via initial outer-sphere one-electron reduction of O_2 to O_2^-, which has been observed experimentally to be $E^0 = 0.4$ V at pH of 13,[64] (Path B), followed by concerted or stepwise adsorption and protonation. The concerted adsorption and protonation, however, is a formally ternary reaction, necessitating that water act at the proton donor. Even in this limit, the concerted adsorption and protonation sequence may be kinetically disfavored relative to the stepwise sequence. As outer-sphere reduction of O_2 is known to be an electrochemically reversible redox process,[65,66] it appears reasonable to expect that this ET remains in quasi-equilibrium in this sequence followed by rate-limiting O_2^- adsorption (Path B). Alternatively, O_2 adsorption and electron transfer may be concerted, with a computed E_0 = 0.2 V (Path C). This electrosorption reaction is then followed by a strongly favorable protonation step, and thus we postulate that electrosorption of O_2 is rate limiting in this sequence. Notably, both pathways B and C would be expected to display a first order dependence in O_2 and a zeroth order dependence in H^+, both of which are qualitatively consistent with our experimental observations (Figure 2). The only distinguishing feature between pathway B and C is the expected dependence of ORR catalytic rate on applied potential. Path B invokes quasi-equilibrium ET followed by a rate limiting chemical step and would therefore be expected to give rise to a 60 mV/decade Tafel slope, which is in line with what we observe experimentally at lower overpotentials. In contrast, Path C invokes rate limiting inner-sphere electron transfer which, assuming a transfer coefficient of 0.5, would be expected to display a 120 mV/decade Tafel slope.[49] As our experimental Tafel data indicates a transition between a ~60 mV/decade region to an ~120 mV/decade region, we postulate that both mechanisms may be viable depending on the applied potential.

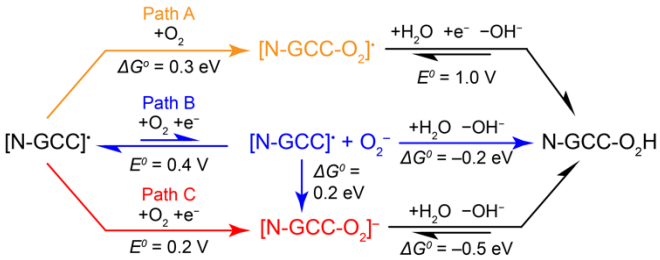

Scheme 2. Computed thermochemistry of various pathways for O_2 activation by N$^+$-GCC active sites. The putative rate-limiting step(s) in each sequence are denoted with irreversible reaction arrows.

Both Paths B and C proceed through a closed shell peroxo intermediate, whereby charge is drawn onto the oxygen as it binds. We use the term peroxo because, after binding, the O–O bond length lengthens to 1.47 Å, longer than the bond length for superoxide (1.28 Å)[67] but quite close to that of peroxide (1.49 Å).[68] This peroxo species also displays a C-O bond length of 1.38 Å, significantly shorter than the corresponding 1.54 Å C–O bond to O_2 in the absence of the additional electron (Path A), suggesting that the bond is stronger as well. The HOMO for the **[N-GCC-O$_2$]$^-$** intermediate is highly localized on the bound oxygen fragment (Figure 5). Likewise, the two oxygen atoms have CHELPG atomic charges[69] of −0.46 and −0.80, indicative of significant charge transfer from the surface, as observed for **[N-GCC-O$_2$]$^\bullet$**.

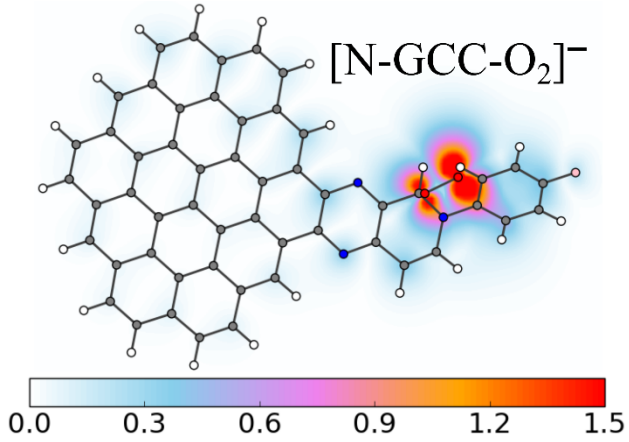

Figure 5. HOMO density plot of **[N-GCC-O_2]$^-$**.

The electrosorption of oxygen is followed by thermodynamically favorable protonation of the bound peroxo species **[N-GCC–O_2]$^-$** to form a bound hydroperoxo intermediate **N-GCC–O_2H**. This step is downhill, with a free energy change of −0.5 eV, even at pH 13. This protonation results in a slight expansion of the C–O bond length from 1.38 to 1.45 Å while the O–O bond length remains roughly constant. The **N-GCC–O_2H** species is closed shell and its HOMO is delocalized over the graphite region of the cluster (Figure 6).

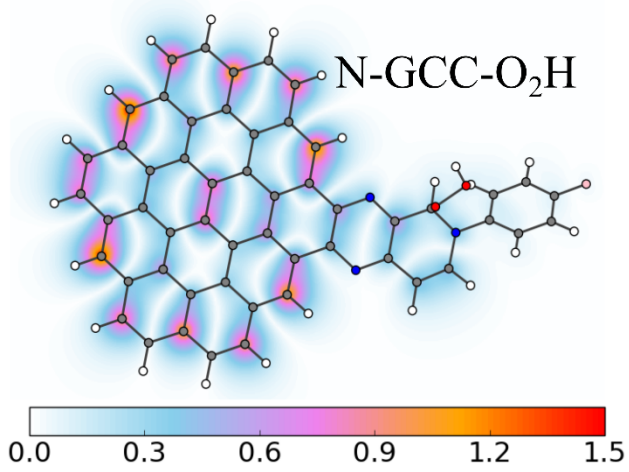

Figure 6. HOMO density plot of **N-GCC-O_2H**.

Subsequent Steps in the Catalytic Cycle (Steps 3-5):
Step 3: Whereas protolytic dissociation of the bound peroxo unit would lead to production of hydrogen peroxide, we found that cleavage of the O–O bond is thermodynamically feasible on **N$^+$-GCC** sites (Scheme 3). Addition of an electron and proton to the hydroperoxo group of **N-GCC-O_2H** leads to the liberation of water and the formation of an oxyl intermediate **[N-GCC-O]$^\bullet$**. Although the latter is a relatively unstable species, the reaction displays a high potential of 1.9 V, driven primarily by the liberation of water. Although the oxyl anion in **[N-GCC-O]$^\bullet$** is bound to a saturated carbon atom, precluding the formation of a C–O double bond, the C–O bond length, nonetheless, shortens to 1.35 Å, indicating partial multiple bond character. The bound oxygen also has appreciable spin density, which is partially delocalized on the surrounding carbon π-system (Figure 7). It is unclear whether this is an artifact of DFT charge delocalization, but it is notably distinct from **[N-GCC-O_2]$^\bullet$** and **[N-GCC-O_2]$^-$**, where essentially no analogous spin or HOMO delocalization was observed.

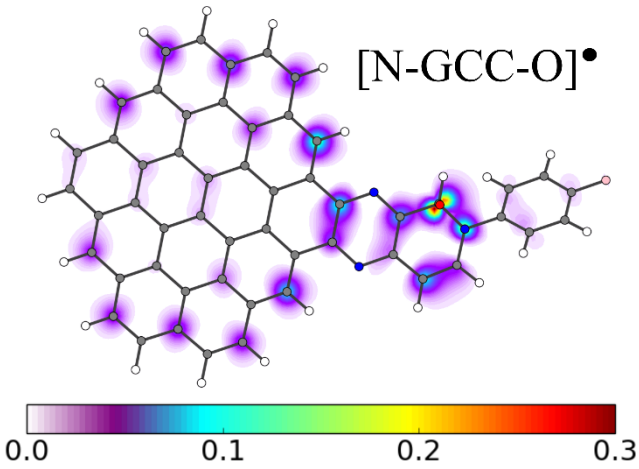

Figure 7. Radical density plot of **[N-GCC-O]$^\bullet$**.

Step 4: The oxyl moiety of **[N-GCC-O]$^\bullet$** undergoes thermodynamically favorable proton-coupled electron transfer (PCET) at 1.6 V to form a bound hydroxo **N–GCC-OH** species (Scheme 3). **N-GCC-OH** is closed shell with a C–O bond length of 1.44 Å, lacking the unstable electronic and molecular features of the previous oxygen-containing intermediate. Much like **N-GCC-O_2H**, **N-GCC-OH**'s HOMO is spread over the graphite region (Figure S4).

Step 5: Finally, electron-proton transfer to the bound hydroxo species, **N-GCC-OH**, liberates water, regenerating **[N-GCC]$^\bullet$** (Scheme 3). Although this step displays a computed formal potential of 0.7 V, placing it within the linear Tafel region (Figure 1), the absence of a Nernstian pH dependence (Figure 2b) indicates that this step lies in intermediate to major equilibrium under the conditions of catalysis.

Overall, the pathway computed here (Scheme 3) has a marked similarity to the associative ORR mechanism, which has been proposed for metal surfaces[63,70–72] as well as disordered N-doped carbons prepared by other methods.[34,36–38,73] Numerous computational studies have concluded that α-carbons bonded to nitrogen dopant sites are preferential sites of O_2 activation in N-doped carbon materials.[7,29,33,36–39,73] Whereas this study uncovers a similar site preference for these well-defined GCC active sites, we find that the initial steps of O_2 activation bifurcate along several proton-independent pathways (Scheme 3) that explain the general observation of inferior ORR activity for metal-free N-doped carbons in acidic electrolytes.[42,43]

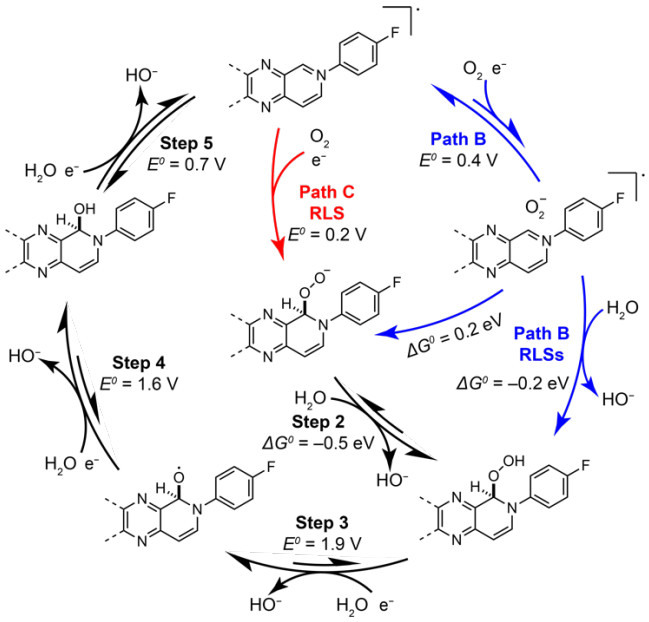

Scheme 3. Proposed catalytic cycle for ORR by [N-GCC]• active sites. All electrochemical potentials, E°, are relative to the reversible hydrogen electrode at pH 13. The thermochemistry of all chemical steps, ΔG°, are adjusted for the chemical activity of H^+/OH^- at pH 13. RLS refers to the rate-limiting step in each sequence with two RLSs depicted in path B (blue).

Comparing Metal and N$^+$-GCC Catalysis with Descriptors

Relative activities for ORR catalysis among metal surfaces have been effectively rationalized using catalyst descriptors, which are one or more characteristics of a set of catalysts that correlate strongly with trends in their activity.[63,74] In particular, a consensus has emerged that ORR activity can be generalized across a wide array of metal surfaces by correlating activity to the relative adsorption strength of O and OH.[63,75,76] Depending on their relative strength of adsorption, three broad regimes emerge (Figure 8). Surfaces that display strong O binding but weak OH binding are limited by reduction of surface O intermediates (Figure 8, bottom right), whereas surfaces that display intermediate to weak O binding and strong OH binding are limited by OH desorption (Figure 8, left). For metals which display weak O and moderate OH adsorption (Figure 8, top), the associative mechanism prevails. In particular, weak O adsorption translates into weak O_2 adsorption, and thus metals like Au and Ag are thought to proceed via a mechanism in which the following O_2 adsorption equilibrium

$$R + O_2 + H^+ + e^- \rightleftarrows R - O_2H \qquad \text{eq. } \mathbf{2}$$

dictates the potential region of catalysis.

Applying this same descriptor analysis to **N$^+$-GCC** reveals that these N-doped carbon moieties lie in the third category, limited by the binding of O_2. The slightly stronger than optimal OH chemisorption paired with the slightly weaker than optimal O_2 adsorption places these N-doped carbon surfaces in a similar region of reactivity to that of Ag (Figure 8), which is itself a potent catalyst for ORR in alkaline media.[77] Remarkably, we do indeed observe that the estimated per site turnover frequencies of **N$^+$-GCC** are comparable to that of polycrystalline Ag, consistent with these broad thermochemical trends.[45]

This analysis provides key insights into catalyst design. In particular, varying the substitution pattern of the N-dopant active site to increase its electrophilicity will improve activity only up to a point. The strongly correlated binding strength of O and OH apparent in Figure 8 is a known scaling relation, which dictates that a more electrophilic active site will lead to enhanced O_2 adsorption, but will also enhance OH adsorption. Thus, **N$^+$-GCC** would need to simultaneously increase O and decrease OH binding strengths to move towards the global optimum at the nexus of the three sectors depicted in Figure 8. Moving in this direction, however, constitutes breaking the scaling relation for oxygen binding strength.[74] As the relation of these bond energies imposes a limit on the activity even at the local optimum apparent in Figure 8,[78] more unconventional options must be considered to further improve the activity of active sites of this type. One proposal is to incorporate secondary sphere elements that preferentially stabilize O_2 adsorption over OH binding, which has been widely advocated for breaking scaling relations in heterogeneous catalysis.[76,79] While this can prove challenging in practice,[80] the molecular fidelity and synthetic tunability afforded by GCCs provides an ideal platform for generating active sites specifically designed to preferentially stabilize O_2 adsorption over OH binding.

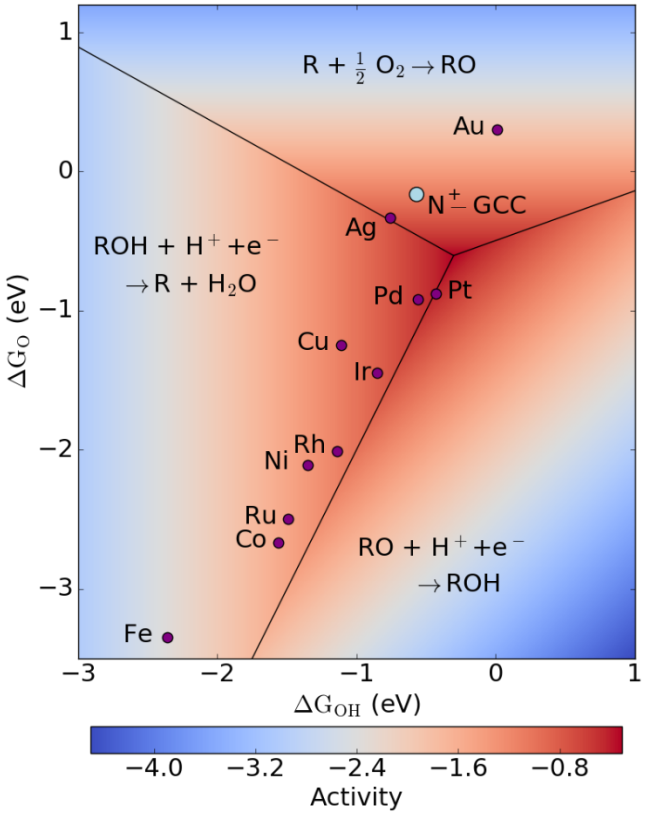

Figure 8. ORR catalytic activity of **N^+-GCC** and metal surfaces based on the dissociative ORR mechanism. The data for metal surfaces, as well as the linear free energy relationship for activity is taken from reference 63.

Conclusions

Using a combination of experimental and computational tools, we have developed a mechanistic model of ORR catalysis by well-defined graphite-conjugated active sites featuring aryl-pyridinium moieties. Electrokinetic data establish a rate law for catalysis that is approximately first order in O_2 partial pressure and near zero order in pH. Tafel analysis suggests an equilibrium electron transfer process following a rate-limiting chemical step at modest overpotentials that transitions to a rate-limiting electron transfer sequence at higher overpotentials. Combining this experimental data with finite-cluster computational modelling of the GCC active sites allows us to assemble a consistent mechanistic model for ORR catalysis that invokes O_2 adsorption at electrophilic carbons alpha to the pyridinium moiety of the GCC fragment. The model invokes rate-controlling O_2 activation steps that are proton de-coupled, explaining the low pH dependence of ORR catalysis that gives rise to inferior activity in acidic media. Consistent with the experimental Tafel data, the model invokes, depending on the applied potential, either concerted or step-wise electron transfer and adsorption of O_2 which is followed by a series of electron/proton transfer steps to generate water and turnover the catalytic cycle. The thermochemical parameters of the GCC active site place it on the associative O_2-binding 'leg' of the ORR volcano plot with properties similar to that of Ag metal. Given the high fidelity and synthetic tunability of GCCs, the mechanistic model developed here serves as a roadmap for the bottom-up synthesis of highly active N-doped carbon ORR catalysts.

ASSOCIATED CONTENT

Supporting Information Available: Detailed synthesis, experimental setup, Koutecky-Levich plots, analysis of size effects of cluster model, comparison of radical localization on other **GCC** fragments. This material is available free of charge via the Internet at http://pubs.acs.org.

AUTHOR INFORMATION

Corresponding Author

*yogi@mit.edu
*tvan@mit.edu

Notes

The authors declare no competing financial interest.

ACKNOWLEDGMENT

This work was supported by the U.S. Department of Energy, Office of Science, Office of Basic Energy Sciences, under award number DE-SC0014176 and by the MIT Department of Chemistry through junior faculty funds for Y.S. A.T.M is support by the Dreyfus Postdoctoral Fellowship.

REFERENCES

(1) Graetzel, M. *Acc. Chem. Res.* **1981**, *14*, 376–384.
(2) Lewis, N. S.; Nocera, D. G. *Proc. Natl. Acad. Sci.* **2006**, *103*, 15729–15735.
(3) Turner, J. A. *Science.* **2004**, *305*, 972–974.
(4) Crabtree, G. W.; Dresselhaus, M. S.; Buchanan, M. V. *Phys. Today* **2004**, *57*, 39–44.
(5) Wang, D.-W.; Su, D. *Energy Environ. Sci.* **2014**, *7*, 576–591.
(6) Dai, L.; Xue, Y.; Qu, L.; Choi, H.-J.; Baek, J.-B. *Chem. Rev.* **2015**, *115*, 4823–4892.
(7) Lai, L.; Potts, J. R.; Zhan, D.; Wang, L.; Poh, C. K.; Tang, C.; Gong, H.; Shen, Z.; Lin, J.; Ruoff, R. S. *Energy Environ. Sci.* **2012**, *5*, 7936.
(8) McCrory, C. C. L.; Jung, S.; Peters, J. C.; Jaramillo, T. F. *J. Am. Chem. Soc.* **2013**, *135*, 16977–16987.
(9) Rossmeisl, J.; Dimitrievski, K.; Siegbahn, P.; Nørskov, J. K. *J. Phys. Chem. C* **2007**, *111*, 18821–18823.
(10) Ni, M.; Leung, M. K. H.; Leung, D. Y. C.; Sumathy, K. *Renew. Sustain. Energy Rev.* **2007**, *11* (3), 401–425.
(11) Garsuch, A.; Bonakdarpour, A.; Liu, G.; Yang, R.; Dahn, J. R. Time to move beyond transition metal-N-C catalysts for oxygen reduction. In *Handbook of Fuel Cells*; Vielstich, W., Lamm, A., Gasteiger, H. A., Yokokawa, H., Eds.; John Wiley & Sons, Ltd: Chichester, UK, 2010, pp 71-80.
(12) Wagner, F. T.; Lakshmanan, B.; Mathias, M. F. *J. Phys. Chem. Lett.* **2010**, *1*, 2204–2219.
(13) Gasteiger, H. A.; Kocha, S. S.; Sompalli, B.; Wagner, F. T. *Appl. Catal. B Environ.* **2005**, *56*, 9–35.
(14) Brinkman, N.; Wang, M.; Weber, T.; Darlington, T. *Well-to-Wheels Analysis of Advanced Fuel/Vehicle Sysems - A North American Study of Energy Use, Greenhouse Gas Emissions, and Criteria Pollutant Emissions.* Argonne National Laboratory: Argonne, IL, **2005**.
(15) Debe, M. K. *Nature* **2012**, *486*, 43–51.
(16) Martin, K. E.; Kopasz, J. P.; McMurphy, K. W. In *Fuel Cell Chemistry and Operation (American Chemical Society Symposium Series)*; 2010; Vol. 1040, pp 1–13.
(17) Chen, S.; Duan, J.; Jaroniec, M.; Qiao, S.-Z. *Adv. Mater.* **2014**, *26*, 2925–2930.
(18) Wu, Z.-S.; Yang, S.; Sun, Y.; Parvez, K.; Feng, X.; Müllen, K. *J. Am. Chem. Soc.* **2012**, *134*, 9082–9085.
(19) Chen, Z.; Higgins, D.; Tao, H.; Hsu, R. S.; Chen, Z. *J. Phys. Chem. C* **2009**, *113*, 21008–21013.
(20) Song, S.; Zhang, H.; Ma, X.; Shao, Z.; Baker, R. T.; Yi, B. *Int. J. Hydrogen Energy* **2008**, *33*, 4955–4961.
(21) Zhang, Y.; Ge, J.; Wang, L.; Wang, D.; Ding, F.; Tao, X.; Chen, W. *Sci. Rep.* **2013**, *3*, 2771.
(22) Gong, K.; Du, F.; Xia, Z.; Durstock, M.; Dai, L. *Science* **2009**, *323*, 760–764.
(23) Subramanian, N. P.; Li, X.; Nallathambi, V.; Kumaraguru, S. P.; Colon-Mercado, H.; Wu, G.; Lee, J.-W.; Popov, B. N. *J. Power Sources* **2009**, *188*, 38–44.
(24) Qu, L.; Liu, Y.; Baek, J.-B.; Dai, L. *ACS Nano* **2010**, *4*, 1321–1326.
(25) Shao, Y.; Zhang, S.; Engelhard, M. H.; Li, G.; Shao, G.; Wang, Y.; Liu, J.; Aksay, I. A.; Lin, Y. *J. Mater. Chem.* **2010**, *20*, 7491.
(26) Wang, B. *J. Power Sources* **2005**, *152*, 1–15.
(27) Morozan, A.; Jousselme, B.; Palacin, S. *Energy Environ. Sci.* **2011**, *4*, 1238.
(28) Ito, Y.; Qiu, H.-J.; Fujita, T.; Tanabe, Y.; Tanigaki, K.; Chen, M. *Adv. Mater.* **2014**, *26*, 4145–4150.
(29) Sidik, R. A.; Anderson, A. B.; Subramanian, N. P.; Kumaraguru, S. P.; Popov, B. N. *J. Phys. Chem. B* **2006**, *110*, 1787–1793.
(30) Vayner, E.; Anderson, A. B. *J. Phys. Chem. C* **2007**, *111*, 9330–9336.
(31) Kurak, K. A.; Anderson, A. B. *J. Phys. Chem. C* **2009**, *113*, 6730–6734.
(32) Rao, C. V.; Cabrera, C. R.; Ishikawa, Y. *J. Phys. Chem. Lett.* **2010**, *1*, 2622–2627.
(33) Kim, H.; Lee, K.; Woo, S. I.; Jung, Y. *Phys. Chem. Chem. Phys.* **2011**, *13*, 17505–17510.
(34) Zhang, L.; Xia, Z. *J. Phys. Chem. C* **2011**, *115*, 11170–11176.

(35) Choi, C. H.; Lim, H.-K.; Chung, M. W.; Park, J. C.; Shin, H.; Kim, H.; Woo, S. I. *J. Am. Chem. Soc.* **2014**, *136*, 9070–9077.
(36) Guo, D.; Shibuya, R.; Akiba, C.; Saji, S.; Kondo, T.; Nakamura, J. *Science* **2016**, *351*, 361–365.
(37) Luo, Z.; Lim, S.; Tian, Z.; Shang, J.; Lai, L.; MacDonald, B.; Fu, C.; Shen, Z.; Yu, T.; Lin, J. *J. Mater. Chem.* **2011**, *21*, 8038–8044.
(38) Yu, L.; Pan, X.; Cao, X.; Hu, P.; Bao, X. *J. Catal.* **2011**, *282*, 183–190.
(39) Li, Q.; Noffke, B. W.; Wang, Y.; Menezes, B.; Peters, D. G.; Raghavachari, K.; Li, L. *J. Am. Chem. Soc.* **2014**, *136*, 3358–3361.
(40) Noffke, B. W.; Li, Q.; Raghavachari, K.; Li, L. *J. Am. Chem. Soc.* **2016**, *138*, 13923–13929.
(41) Devanathan, R. *Energy Environ. Sci.* **2008**, *1*, 101–119.
(42) Kong, X.-K.; Chen, C.-L.; Chen, Q.-W. *Chem. Soc. Rev.* **2014**, *43*, 2841–2857.
(43) Wang, H.; Maiyalagan, T.; Wang, X. *Acs Catal.* **2012**, *2*, 781–794.
(44) Li, Q.; Zhang, S.; Dai, L.; Li, L. *J. Am. Chem. Soc.* **2012**, *134*, 18932–18935.
(45) Fukushima, T.; Drisdell, W.; Yano, J.; Surendranath, Y. *J. Am. Chem. Soc.* **2015**, *137*, 10926–10929.
(46) Thorogood, C. A.; Wildgoose, G. G.; Crossley, A.; Jacobs, R. M. J.; Jones, J. H.; Compton, R. G. *Chem. Mater.* **2007**, *19*, 4964–4974.
(47) Wildgoose, G. G.; Abiman, P.; Compton, R. G. *J. Mater. Chem.* **2009**, *19*, 4875–4886.
(48) Oh, S.; Gallagher, J. R.; Miller, J. T.; Surendranath, Y. *J. Am. Chem. Soc.* **2016**, *138*, 1820–1823.
(49) Gileadi, E. *Physical electrochemistry: fundamentals, techniques and applications*; Wiley-VCH: Weinheim, Germany, 2011; pp 29-92.
(50) Hohenberg, P. *Phys. Rev.* **1964**, *136*, B864–B871.
(51) Kohn, W.; Sham, L. J. *Phys. Rev.* **1965**, *140*, A1133–A1138.
(52) Fazio, G.; Ferrighi, L.; Perilli, D.; Di Valentin, C. *Int. J. Quantum Chem.* **2016**, *116*, 1623–1640.
(53) Y. Shao, Z. Gan, E. Epifanovsky, A. T. B. Gilbert, M. Wormit, J. Kussmann, A. W. Lange, A. Behn, J. Deng, X. Feng, D. Ghosh, M. Goldey P. R. Horn, L. D. Jacobson, I. Kaliman, R. Z. Khaliullin, T. Kús, A. Landau, J. Liu, E. I. Proynov, Y. M. Rhee, R. M. Ri, Head-Gordon, M. *Mol. Phys.* **2015**, *113*, 184–215.
(54) Becke, A. D. *J. Chem. Phys.* **1993**, *98*, 5648.
(55) Lee, C.; Yang, W.; Parr, R. G. *Phys. Rev. B* **1988**, *37*, 785–789.
(56) Cances, E.; Mennucci, B.; Tomasi, J. *J. Chem. Phys.* **1997**, *107*, 3032.
(57) Chipman, D. M. *J. Chem. Phys.* **2000**, *112*, 5558–5565.
(58) Frisch, M. J.; Pople, J. A.; Binkley, J. S. *J. Chem. Phys.* **1984**, *80*, 3265–3269.
(59) Ditchfield, R.; Hehre, W. J.; Pople, J. A. *J. Chem. Phys.* **1971**, *54*, 724–728.
(60) Clark, T.; Chandrasekhar, J.; Spitznagel, G. W.; Schleyer, P. V. R. *J. Comput. Chem.* **1983**, *4*, 294–301.
(61) Hehre, W. J.; Ditchfield, R.; Pople, J. A. *J. Chem. Phys.* **1972**, *56*, 2257–2261.
(62) Mavros, M. G.; Tsuchimochi, T.; Kowalczyk, T.; McIsaac, A.; Wang, L.-P.; Voorhis, T. Van. *Inorg. Chem.* **2014**, *53*, 6386–6397.
(63) Nørskov, J. K.; Ressmeisl, J.; Logadottir, A.; Lindqvist, L.; Kitchin, J. R.; Bligaard, T.; Jonsson, H. *J. Phys. Chem. B* **2004**, *108*, 17886–17892.
(64) Wood, P. M. *Biochem. J.* **1988**, *253*, 287–289.
(65) Yang, H.-H.; McCreery, R. L. *J. Electrochem. Soc.* **2000**, *147*, 3420.
(66) Zhang, C.; Fan, F.-R. F.; Bard, A. J. *J. Am. Chem. Soc.* **2009**, *131*, 177–181.
(67) Abrahams, S. C.; Kalnajs, J. *Acta Crystallogr.* **1955**, *8*, 503–506.
(68) Holleman, A. F.; Wiberg, E.; Wiberg, N. *Inorganic Chemistry*; Academic Press: New York, NY, 2001; pp 1477.
(69) Breneman, C. M.; Wiberg, K. B. *J. Comput. Chem.* **1990**, *11*, 361–373.
(70) Su, H.-Y.; Gorlin, Y.; Man, I. C.; Calle-Vallejo, F.; Nørskov, J. K.; Jaramillo, T. F.; Rossmeisl, J. *Phys. Chem. Chem. Phys.* **2012**, *14*, 14010–14022.
(71) Nilekar, A.; Udaykumar; Mavrikakis, M. *Surf. Sci.* **2008**, *602*, L89–L94.
(72) Viswanathan, V.; Hansen, H. A.; Rossmeisl, J.; Nørskov, J. K. *J. Phys. Chem. Lett.* **2012**, *3*, 2948–2951.
(73) Okamoto, Y. *Appl. Surf. Sci.* **2009**, *256*, 335–341.
(74) Abild-Pedersen, F.; Greeley, J.; Studt, F.; Rossmeisl, J.; Munter, T. R.; Moses, P. G.; Skúlason, E.; Bligaard, T.; Nørskov, J. K. *Phys. Rev. Lett.* **2007**, *99*, 16105.
(75) Nørskov, J. K.; Bligaard, T.; Logadottir, A.; Bahn, S.; Hansen, L. B.; Bollinger, M.; Bengaard, H.; Hammer, B.; Sljivancanin, Z.; Mavrikakis, M.; others. *J. Catal.* **2002**, *209*, 275–278.
(76) Man, I. C.; Su, H.-Y.; Calle-Vallejo, F.; Hansen, H. A.; Martínez, J. I.; Inoglu, N. G.; Kitchin, J.; Jaramillo, T. F.; Nørskov, J. K.; Rossmeisl, J. *ChemCatChem* **2011**, *3*, 1159–1165.
(77) Alia, S. M.; Duong, K.; Liu, T.; Jensen, K.; Yan, Y. *ChemSusChem* **2012**, *5*, 1619–1624.
(78) Koper, M. T. M. *J. Electroanal. Chem.* **2011**, *660*, 254–260.
(79) Calle-Vallejo, F.; Martínez, J. I.; Rossmeisl, J.; Lindqvist, L.; Kitchin, J. R.; Bligaard, T.; Jonsson, H.; Hinnemann, B.; Rossmeisl, J.; Bligaard, T.; Nørskov, J. K.; Nilsson, A. *Phys. Chem. Chem. Phys.* **2011**, *13*, 15639.
(80) Baran, J. D.; Grönbeck, H.; Hellman, A. *J. Am. Chem. Soc.* **2014**, *136*, 1320–1326.

Insert Table of Contents artwork here